From the holdings of the Department of Special Collections , Princeton University Library, Princeton, NJ

These documents are either in the public domain, or can only be used for educational and research purposes (Fair use) as per U.S. Copyright law (text below). By accessing this file, all users agree that their use falls in the public domain or within fair use as defined by the copyrightlaw. We do not charge any permission or usage fees for the publication of images of material inour collections, including those provided by Princeton University Library, via our website, catalog, or directly from staff.For more information regarding copyright, credit, and citation please review the information onthe Copyright, Credit and Citation Guidelines page of our website.
https://library.princeton.edu/special-collections/policies/copyright-credit-and-citation-guidelines. If you have any questions, including how to order higher-quality images from the collection, contact Special Collections Public Services via our Ask Us! Form. https://library.princeton.edu/special-collections/ask-us

---

Master's Theses, 2022-2026 Electrical and Computer Engineering

2025

Local Control Techniques for Quantum Computing with Yb-171 Tweezer Arrays

Clothier, Caleb

Princeton, NJ : Princeton University

---

http://arks.princeton.edu/ark:/88435/dsp01zs25xc93p

U.S. Copyright law: The copyright law of the United States (Title 17, §108, United States Code) governs the making of photocopies or other reproductions of copyrighted material. Under certain conditions specified in the law, libraries and archives are authorized to furnish a photocopy or other reproduction. One of these specified conditions is that the photocopy or reproduction is not to be used for any purpose other than private study, scholarship, or research. If a user makes a request for, or later uses, a photocopy or reproduction for purposes in excess of fair use that user may be liable for copyright infringement. This institution reserves the right to refuse to accept a copying order if, in its judgment, fulfillment of the order would involve a violation of copyright law. https://www.copyright.gov/title17/title17.pdf

Local Control Techniques for Quantum Computing with Yb-171 Tweezer Arrays

Caleb Clothier

Advisor: Jeff Thompson

Submitted in partial fulfillment

of the requirements for the degree of

Master of Science in Engineering

Department of Electrical and Computer Engineering

Princeton University

May 2025

I hereby declare that I am the sole author of this thesis.

I authorize Princeton University to lend this thesis to other institutions or individuals for the purpose of scholarly research.



Caleb Clothier

I further authorize Princeton University to reproduce this thesis by photocopying or by other means, in total or in part, at the request of other institutions or individuals for the purpose of scholarly research.



Caleb Clothier

Abstract

Neutral atom tweezer arrays are a promising emerging platform for scalable quantum computation. This thesis elaborates a scheme for implementing locally-addressed single-qubit phase gates in a Yb-171 tweezer array, using light shifts on selected sites to detune the Raman transition used to perform the phase gate. The use of acousto-optic deflectors for generating both trapping and addressing beams introduces spurious intermodulation effects, which can cause unwanted crosstalk and degrade gate fidelity. These effects are analyzed both theoretically and experimentally, demonstrating that intermodulation products scale cubically with diffraction efficiency and can be suppressed by operating at low efficiency. Theoretical analysis and master equation simulations incorporating intermodulation show that high-fidelity local phase gates (with infidelity $\sim 10^{-4}$) are achievable with modest addressing laser detuning and power. To enable future implementation, a 497nm laser system was designed and constructed. These results establish a viable pathway toward high-fidelity, site-resolved single-qubit phase gates in Yb-171.

Acknowledgements

I would first like to thank my advisor, Jeff, for his guidance and insight throughout this project. Working in Jeff's group has been an intellectually formative experience, and I am deeply grateful for the opportunity to be a member of his lab.

I owe a special thanks to my labmates Genyue, Bichen, and Sebastian. Their patience, expertise, and generosity with their time taught me so much of the atomic physics I now know, and their mentorship was essential in every stage of this thesis.

To my friends Marti, Andrew, and Benedikt – thank you for making graduate school genuinely fun. You made the hard days easier and the good ones even better.

Finally, I'm grateful to everyone whose support, in ways big and small, helped make this work possible.

Contents

Abstract iii

Acknowledgements iv

List of Figures vii

1 Introduction to Yb-171 Tweezer Arrays **1**

1.1 Outline of thesis 1

1.2 Key experimental techniques 2

1.2.1 Optical trapping 2

1.2.2 Rydberg states 3

1.3 Quantum computing with Yb-171 4

1.3.1 Alkaline-earth atoms 4

1.3.2 Experimental platform 5

2 Acousto-Optic Deflectors **8**

2.1 Theory of the acoustic-optic effect 8

2.1.1 Wavevector picture 9

2.1.2 Diffraction efficiency 11

2.2 Intermodulation in acousto-optic devices 12

2.2.1 Rediffraction 13

2.2.2 Acoustic nonlinearity 14

2.2.3 Experimental characterization in TeO_2 slow-shear mode AOD 14

2.3 Acoustic phonon dispersion 18

3 Local Phase Gates with Light Shifts in Yb-171 **21**

3.1 Local Rydberg phase gate 22

3.2 Raman phase gate with local light shifts 23

3.2.1 Raman transition: $^3P_0 \rightarrow {}^3S_1 \rightarrow {}^3P_2$ 24

3.2.2 Light shifts: $^3P_2 \rightarrow {}^3D_2$ 26

3.2.3 Master equation simulations 28

3.3 497nm laser system 32

3.3.1 AOM and fiber coupling setup 32

3.3.2 Local addressing setup 34

3.3.3 Future steps 36

List of Figures

1.1 Partial energy level diagram for ^{171}Yb showing key states, transitions, and lifetimes, adapted from Ref. [1]. 5

1.2 All figures are adapted from Ref. [2]. (a) Pumping scheme for metastable qubit initialization in $|1\rangle$. (b) Level diagram depicting single- and two-qubit operations, as well as imaging transitions. (c) Blowout and depumping scheme for metastable qubit readout. 7

2.1 Diagram of a typical acousto-optic device operating in the Bragg regime, adapted from Zeng et al. (2009). 10

2.2 (a) Isotropic plane wave interaction, only one frequency exactly obeys phase-matching condition. The diffraction efficiency decreases with increased phase mismatch Δk. (b) Isotropic interaction with finite single-frequency bandwidth determined by transducer lineshape. (c) Anisotropic interaction, with two frequencies exactly obeying phase-matching condition. 11

2.3 Multiple rediffraction for two driving frequencies f_1 and f_2. The dashed lines illustrate the scattering events that produce one of the two-tone third order intermodulation products. 13

2.4 (a) Measured DTSXY-400-532 single-axis diffraction efficiency at 497nm (relative to peak efficiency to match the datasheet). (b) Plot provided by AA-Optoelectronics for the DTSXY-400-532 diffraction efficiency. The two blue curves correspond to the 1st and 2nd order efficiencies at 497nm. 15

2.5 The measured first-order and third-order intermodulation powers are plotted on the left, normalized by the maximum measured power. The power law fits are $P_{\text{first-order}} \propto P^{1.01(7)}$ and $P_{\text{intermod}} \propto P^{2.92(2)}$, where the fits are performed in the low power regime to exclude nonlinearity due to efficiency saturation. The intermod rejection $R = 10\log_{10}(P_{\text{first-order}}/P_{\text{intermod}})$ is plotted on the right against the diffraction efficiency. 16

2.6 (a) Experimental setup for simultaneous imaging of zeroth- and first-order diffracted beams. (b) Unprocessed camera image showing cross-shaped diffraction pattern associated with the acoustic phonon dispersion of the slow-shear mode in paratellurite 17

2.7 (a) Plot of acoustic slowness $1/v$ in the (001) plane for the slow-shear mode in paratellurite. The transducer launches acoustic waves at a small angle with the (110) axis, where the acoustic velocity reaches a minimum of 650 m/s. (b) Log-scale image of zeroth- and first-order diffracted beams for two acoustic drive frequencies, 77 and 97 MHz. The predicted diffraction patterns are plotted in blue and orange, showing close agreement with the observed patterns. The second-order intermodulation products are also visible around the zeroth-order beam, illustrating the process of rediffraction. 18

2.8 Power profile along the acoustic phonon dispersion pattern. The central peak corresponds to the first-order diffraction product, with power decreasing away from the center frequency like $\sim 1/(\Delta f)^2$, consistent with the expected spectral envelope for a square transducer. The spurious power remains greater than -40dB within a $\Delta f = \pm 2$ MHz region around the center frequency. . . 19

3.1 Level diagram depicting the current scheme for local phase gates using the 302nm Rydberg transition, and an illustration of local addressing based on atom transport. 22

3.2 Level diagram illustrating the proposed scheme for performing local phase gates, with global 649nm and 770nm beams that drive a Raman transition and local 497nm beams that light-shift the Raman transition out of resonance at selected sites. 23

3.3 (a) Simulated gate infidelity $1 - \bar{F}$ for addressed ("bright") and unaddressed ("dark") sites as a function of the light shift on the Raman transition. (b) Ratio of intermodulation power to first-order power in dBc required to achieve a target gate infidelity, determined by equating the dark and bright infidelities and calculating the ratio between the respective light shifts. 29

3.4 (a) Average of the simulated gate infidelities $1 - \bar{F}$ for addressed and unaddressed sites, using an intermodulation rejection ratio $r = 10^{-4}$. The infidelity increases when using large Rabi frequencies due to intermodulation, and when using large detunings due to smaller resulting light shifts. (b) Minimal gate infidelity curve for the 2D parameter sweep, compared with the curve of constant light shift $\Delta_{LS} = \Omega^2/4\Delta \sim 2\pi \times 75$ MHz. (c) Average gate infidelity along the minimal curve, plotted as a function of detuning. 30

3.5 Diagram of the experimental setup for frequency-shifting and fiber-coupling 497nm light for local addressing, depumping, and frequency stabilization. . . 34

3.6 Diagram of the local addressing breadboard and combination pathway with AOD/SLM tweezers, and a CAD model of the entire tweezer + addressing setup. 35

Chapter 1

Introduction to Yb-171 Tweezer Arrays

Neutral atom tweezer arrays have rapidly matured into a promising experimental platform for quantum science. In particular, the ability to control individual atoms and perform entangling operations across multiple atoms at scale provides a novel approach to quantum information processing. Recent advancements have enabled demonstrations of high-fidelity entangling gates [3], programmable quantum processors [4], and quantum error correction with logical qubits [5].

1.1 Outline of thesis

This thesis primarily focuses on the development of a novel method for performing locally-addressed single-qubit phase gates. It is organized into three sections. Chapter 1 introduces the field of neutral atom quantum computing and describes the existing experimental setup based on ^{171}Yb atoms, providing context for the contributions of this thesis. Chapter 2 delves into the theory and operation of acousto-optic deflectors, focusing on spurious effects that can limit local addressing fidelity as well as techniques for mitigation. Chapter 3 presents an analysis of the proposed scheme for performing local phase gates and discussion of the

experimental setup.

1.2 Key experimental techniques

1.2.1 Optical trapping

The assembly of large-scale arrays of trapped atoms is a foundational capability in neutral atom experiments. Atom trapping employs the AC Stark effect, in which electromagnetic radiation at a frequency detuned from an atomic transition induces energy-level shifts or "light shifts" on the atomic ground and excited states. In the far-detuned regime, the ground state light shift is given by:

$$\Delta_{LS} = \frac{\Omega^2}{4\Delta} \tag{1.1}$$

where Ω is the transition Rabi frequency and Δ is the detuning. For red-detuned light ($\Delta < 0$), the ground state energy shift is negative. The Rabi frequency depends on the dipole matrix element $\mathbf{d}$ of the transition and the electric field amplitude $\mathbf{E}$:

$$\Omega = \frac{\mathbf{E}(\mathbf{r}) \cdot \mathbf{d}}{\hbar} \tag{1.2}$$

Tightly focusing a red-detuned laser addressing a ground-state transition thus produces a spatially varying electric field profile, leading in turn to a light-shift-induced 3D potential well experienced by the atomic ground state. Since the resulting potential depth is typically in the MHz range for a few mW of laser power, corresponding to an atomic temperature of $T = U/k_B \sim 100\mu\text{K} - 1\text{mK}$, atom cooling is necessary prior to trap loading. Single-atom loading in optical tweezers, first demonstrated in Ref. [6], relies on photoassociation, where light-assisted collisions project the atom number in each trap to either zero or one. This stochastic process yields arrays with roughly half the sites filled, which are then imaged and rearranged via trap movement to create defect-free arrays.

Large-scale tweezer arrays are generated using two key technologies: acousto-optic deflec-

tors (AODs) and spatial light modulators (SLMs). AODs, discussed in detail in Chapter 3, exploit the acousto-optic effect to diffract a single incident laser beam into row- and column-addressed arrays. With microsecond-scale response times and continuous beam-steering capabilities, AODs enable the creation of movable traps, facilitating trap rearrangement and atom transport. SLMs, in contrast, shape the wavefront of an incident laser beam to create arbitrary trap configurations beyond the row/column structure achievable with AODs. However, their slow refresh rate (∼30Hz) limits their use to static trap generation. Altogether, these technologies enable the creation of large tweezer arrays trapping thousands of individual atoms [7].

1.2.2 Rydberg states

Another crucial component of neutral atom systems is the generation and control of multi-atom interactions. While ions interact strongly at large separations through electrostatic repulsion, neutral atoms do not appreciably interact in their low-lying electronic states, largely due to their angstrom-scale electronic wavefunctions. However, Rydberg states with high principal quantum number n have significantly larger wavefunctions. Such large electronic clouds of Rydberg states are highly polarizable, leading to a van der Waals interaction between Rydberg atoms that scales like:

$$U_{vdW} = \frac{C_6}{r^6} \propto n^{11} \tag{1.3}$$

where r is the interatomic separation and C_6 is the van der Waals interaction strength [8]. At experimentally-achievable interatomic distances of several micrometers and moderately high n Rydberg states, this interaction is strong enough to prevent the excitation of multiple nearby atoms to the Rydberg state, an effect known as the Rydberg blockade [9]. The blockade effect can be used to generate entanglement between atoms, enabling operations such as controlled-phase gates [3].

1.3 Quantum computing with Yb-171

1.3.1 Alkaline-earth atoms

Neutral atom tweezer experiments were first developed using alkali atoms such as Rb and Cs, largely due to the simple level structure provided by their single valence electron. Recent experiments have explored the use of alkaline-earth atoms with two valence electrons like Sr [10, 11] and Yb [12], offering a richer electronic structure with long-lived nuclear spin states, metastable clock states, and both strong and narrow optical ground-state transitions [13].

This thesis focuses on an experimental platform using ^{171}Yb, an alkaline-earth-like isotope with nuclear spin $I = 1/2$. A partial energy level diagram is shown for reference in Fig. 1.1. Given the absence of hyperfine coupling in the $^1S_0$ ground state and $^3P_0$ metastable state with zero total electronic angular momentum, the $I = 1/2$ nuclear spin in these manifolds offers a natural qubit encoding with significantly reduced magnetic field sensitivity (owing to the small nuclear magnetic moment $\mu_B/\mu_N \sim 2000$) and vanishing tweezer-induced differential light shift between the nuclear spin sublevels, leading to high coherence.

Encoding qubits in the nuclear spin of the $^3P_0$ metastable state offers several advantages over $^1S_0$ ground state qubits. First, direct single-photon excitation from the metastable state to Rydberg states can enable faster, higher-fidelity control than the two-photon Raman transitions required from the ground state [14]. Second, fast (destructive) mid-circuit readout can be performed through selective transfer to the ground state and imaging on the strong $^1S_0 \rightarrow {}^1P_1$ transition, leaving the population in the metastable state unaffected. And third, decays to the ground state – a dominant error mechanism – can be detected as leakage or "erasure" errors, which have lower thresholds for quantum error correction than general Pauli errors [2, 15].

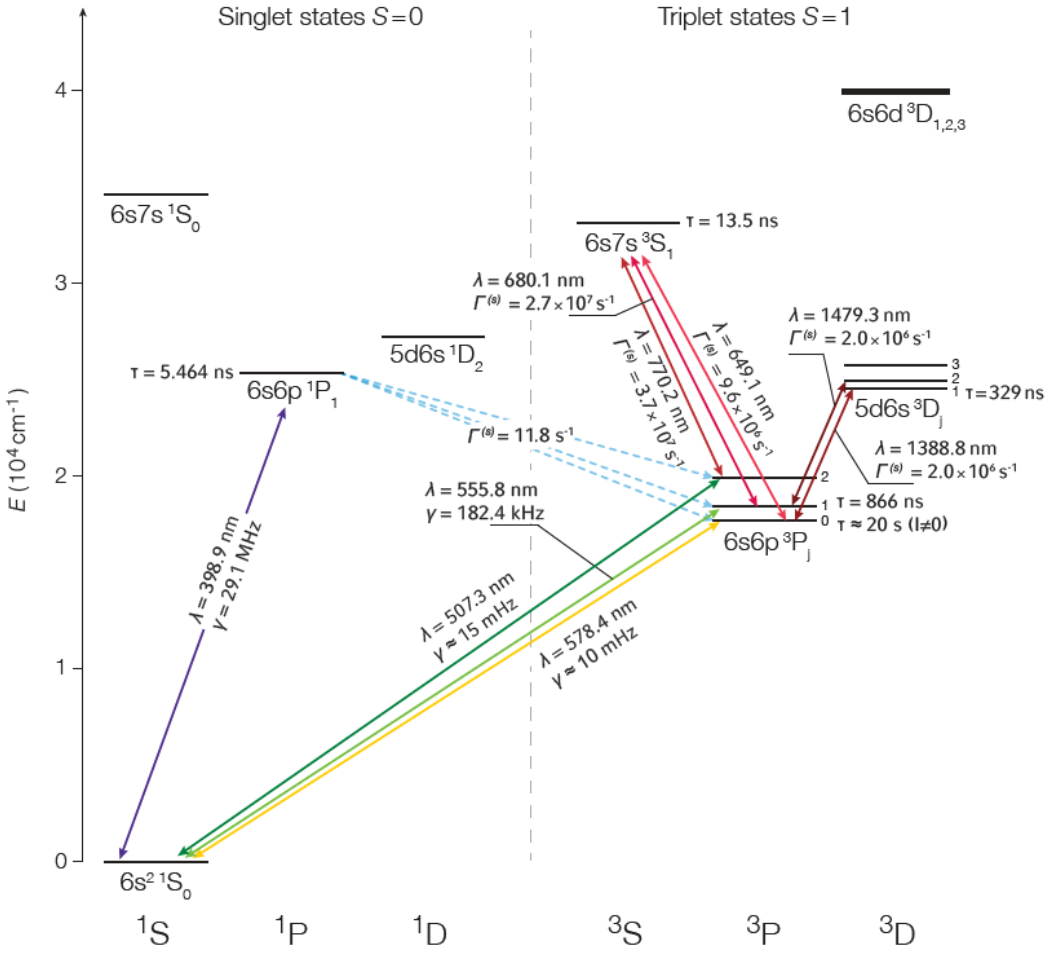


Figure 1.1: Partial energy level diagram for ^{171}Yb showing key states, transitions, and lifetimes, adapted from Ref. [1].

1.3.2 Experimental platform

The setup for cooling and trapping Yb atoms was initially demonstrated by Ref. [12] for the ^{174}Yb isotope. To begin each experiment, a hot beam of Yb atoms is produced by an oven and Doppler-cooled using a 2D magneto-optical trap (MOT) operating on the strong $^1S_0 \rightarrow {}^1P_1$ transition at 399nm. The atoms are subsequently pushed into a glass vacuum chamber and trapped in a 3D MOT operating on the narrow $^1S_0 \rightarrow {}^3P_1$ transition at 556nm for further Doppler cooling to $\sim 5\mu$K. Next, atoms are loaded into optical tweezers at 486nm, a magic wavelength chosen due to the vanishing differential light shift between $^1S_0$ and $^3P_1$

(i.e., the trapping potentials are identical for the two states), which mitigates atom heating during imaging on this intercombination transition. Two overlapping tweezer patterns are produced: "static" tweezers using a spatial light modulator, and "movable" tweezers using a pair of orthogonal acousto-optic deflectors. These beams are combined and focused to a diffraction-limited beam waist of ~ 500nm using a 0.6 NA objective. The trapped atoms are then imaged non-destructively using the intercombination transition to determine tweezer occupation, and rearrangement is performed with the movable AOD tweezers to produce a 1D defect-free array.

The next stage is qubit initialization in the metastable state, described in detail in Ref. [2]. Direct excitation from ${}^1S_0 \rightarrow {}^3P_0$ is difficult due to the extremely narrow linewidth of the transition, and requires tweezers at a magic wavelength. Thus an alternative method is implemented, involving optical pumping through intermediate states. Population transfer to the metastable state is achieved by driving a two-photon transition ${}^1S_0 \rightarrow {}^3P_1 \rightarrow 5d6s\ {}^3D_1$, $F = 3/2$ using σ^+-polarized 556nm and π-polarized 1539nm beams. 64% of the population in ${}^3D_1$ decays back to ${}^3P_0$, with the remaining population decaying to ${}^3P_1$ and ${}^3P_2$. A 770nm beam is used to repump ${}^3P_2 \rightarrow 6s7s\ {}^3S_1$, since ${}^3P_2$ is strongly anti-trapped in the 486nm tweezers. Spin polarization of the ${}^3P_0$ population into the $m_F = 1/2$ state is achieved using a σ^+-polarized 649nm beam addressing the $|{}^3P_0, m_F = -1/2\rangle \rightarrow |{}^3S_1, F = 1/2, m_F = 1/2\rangle$ transition, which selectively removes population in the $m_F = -1/2$ state while leaving the $m_F = 1/2$ population untouched due to selection rules. This pumping sequence yields qubits initialized with high fidelity $> 97\%$ in the $|{}^3P_0, m_F = 1/2\rangle \equiv |1\rangle$ state [2].

Global single-qubit rotations are driven using an RF magnetic field. The static magnetic field $|B| = 5$ G induces a Zeeman splitting between the nuclear spin levels $|0\rangle \equiv |{}^3P_0, m_F = -1/2\rangle$ and $|1\rangle \equiv |{}^3P_0, m_F = 1/2\rangle$, giving a qubit Larmor frequency of $\omega_L = 2\pi \cdot 5.7$ kHz. Two-qubit gates are achieved using a 302nm UV beam that drives a single-photon transition from the metastable state to the Rydberg state $|\nu = 54.3, S, F = 1/2\rangle$. The UV beam drives σ^+ and σ^- transitions, and is tuned on resonance with the $|1\rangle \rightarrow$

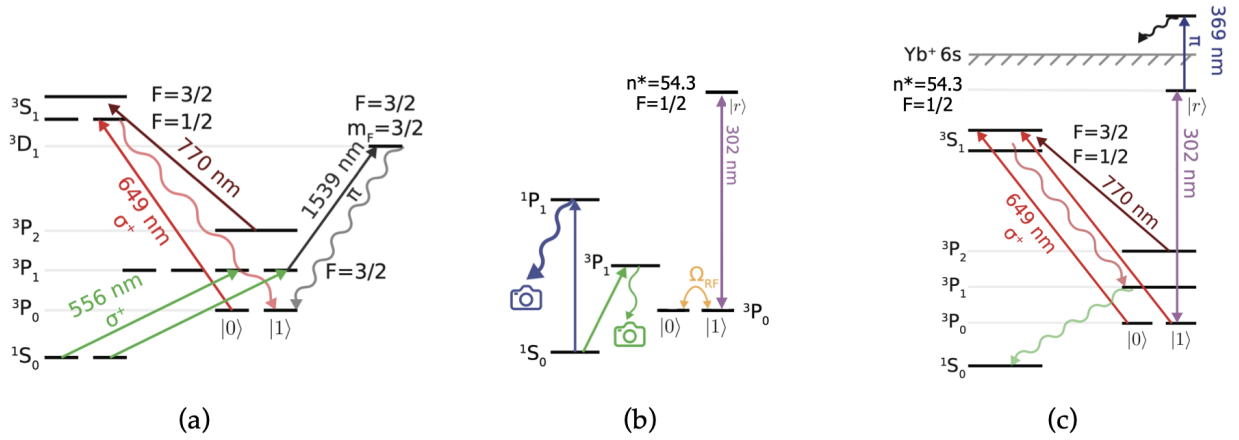


Figure 1.2: All figures are adapted from Ref. [2]. (a) Pumping scheme for metastable qubit initialization in $|1\rangle$. (b) Level diagram depicting single- and two-qubit operations, as well as imaging transitions. (c) Blowout and depumping scheme for metastable qubit readout.

$|n^* = 54.3, S, F = 1/2, m_F = -1/2\rangle$ transition to selectively excite the $|1\rangle$ state. The UV beam waist is located in a "gate zone" region adjacent to the "storage zone" (where atom loading, single-qubit rotations, and readout are performed). To perform site-selective CZ gates, atoms are shuttled to the gate zone, paired to form dimers separated by $\sim 2\mu$m (within the Rydberg blockade radius), and illuminated by an amplitude- and phase-shaped UV pulse.

Two fluorescence imaging techniques are used, depending on the measurement context. Imaging on the strong $^1S_0 \rightarrow {}^1P_1$ transition enables fast ($\sim 20\mu$s) destructive measurement of ground-state population, and is used for mid-circuit detection of erasure errors. In contrast, imaging on the narrow $^1S_0 \rightarrow {}^3P_1$ intercombination line allows for a high-fidelity, non-destructive (albeit slower $\sim$15ms) measurement, and is used for tweezer rearrangement and qubit state readout. The latter requires state-selective depumping from $^3P_0 \rightarrow {}^1S_0$. This is achieved by removing atoms in the $|1\rangle$ state from the trap through selective excitation to the Rydberg state and subsequent auto-ionization with 369nm light. The remaining atoms in the $|0\rangle$ state are then depumped to the ground state through $^3S_1$ in a two-photon process using 649nm and 770nm light.

Chapter 2

Acousto-Optic Deflectors

Aousto-optic devices are a foundational technology in neutral atom quantum computing, enabling operations like fast beam switching, frequency shifting, pulse amplitude shaping, creation of dynamically reconfigurable tweezer arrays, and local addressing. In this chapter, we present the theoretical underpinnings of these devices, with particular attention to spurious effects such as intermodulation and acoustic phonon dispersion, culminating in their experimental characterization. These results inform the analysis of a local addressing scheme using AODs, presented in Chapter 3.

2.1 Theory of the acoustic-optic effect

The acousto-optic effect, originally proposed by Brillouin in 1922 and verified experimentally by Debye and Sears in 1932, describes the diffraction of light due to interaction with sound waves [16]. It is closely analogous to Bragg diffraction of X-rays in a crystalline material, in which light scatters off planes of atoms in the lattice, leading to constructive interference at certain incidence angles where the optical path between adjacent planes is an integer multiple of the wavelength. This process is described by Bragg's law:

$$q\lambda = 2d\sin\theta \tag{2.1}$$

where λ is the wavelength of light, d is the lattice spacing, θ is the angle of incidence, and $q \in \mathbb{Z}$ is the order of the diffracted beam. Although in acousto-optics, the periodic modulation responsible for light diffraction arises from the compression and rarefaction of the acoustic medium rather than from the atomic lattice itself, the geometric analogy to X-ray diffraction provides a useful heuristic framework for approximate understanding of the phenomenon; simply exchanging the lattice spacing d with the acoustic wavelength Λ yields the equation describing the critical Bragg angle for acousto-optic diffraction:

$$\sin\theta_B = \frac{\lambda}{2\Lambda} = \frac{\lambda f}{2v} \tag{2.2}$$

where f and v are the acoustic frequency and velocity, respectively. There are two regimes for acousto-optic interaction: the Bragg regime for large interaction lengths compared to the acoustic wavelength, in which most power is concentrated in a single diffracted order at the Bragg angle, and the Raman-Nath regime for comparatively short interaction lengths, in which multiple diffracted orders with comparable power are produced. This chapter focuses on the Bragg regime, which is utilized by most acousto-optic devices. Figure 2.1 depicts a typical acousto-optic device operating in the Bragg regime.

2.1.1 Wavevector picture

Several frameworks exist for describing the acousto-optic effect, notably the classical perspective of an acoustic strain-induced refractive index grating originally formulated by Brillouin. However, the most intuitive interpretation views the effect in a quantum-mechanical light as arising from the scattering of photons by acoustic phonons, as depicted in Figure 2.2. Denoting the momentum wavevectors for the incident photon, acoustic phonon, and diffracted photon plane waves by $\mathbf{k}$, $\mathbf{K}$, and $\mathbf{k}'$ respectively, conservation of momentum yields the

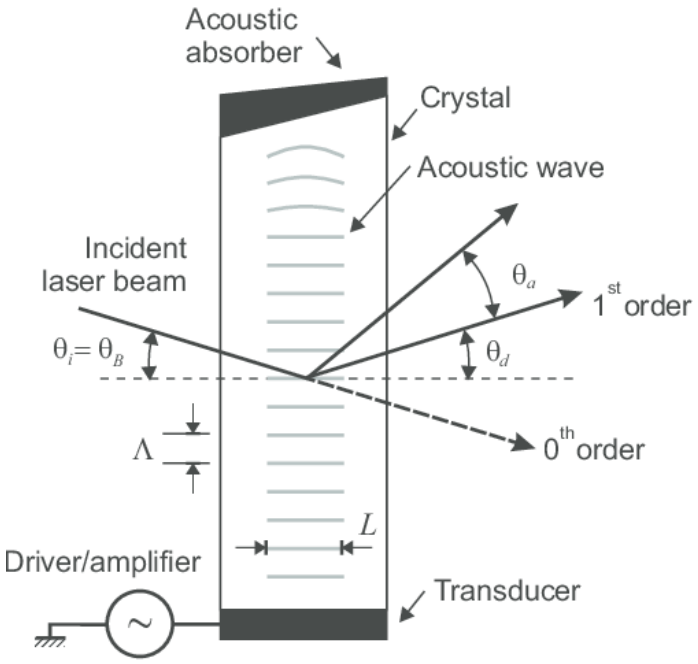


Figure 2.1: Diagram of a typical acousto-optic device operating in the Bragg regime, adapted from Zeng et al. (2009).

following equation for phase-matched phonon absorption/emission:

$$\mathbf{k} \pm \mathbf{K} = \mathbf{k}' \tag{2.3}$$

Conservation of energy yields a corresponding frequency shift, where ω, Ω, and ω' are the frequencies of the incident photon, acoustic phonon, and diffracted photon respectively:

$$\omega \pm \Omega = \omega' \tag{2.4}$$

Since the optical frequencies are much larger than the acoustic frequencies $\omega \gg \Omega$, the diffracted photon wavevector magnitude is approximately unchanged $k' = \omega'/v \approx \omega/v = k$, producing an isosceles wavevector diagram with base K and side length k from which Eq. (2.2) is readily recovered:

$$\sin\theta_B = \frac{K}{2k} \tag{2.5}$$

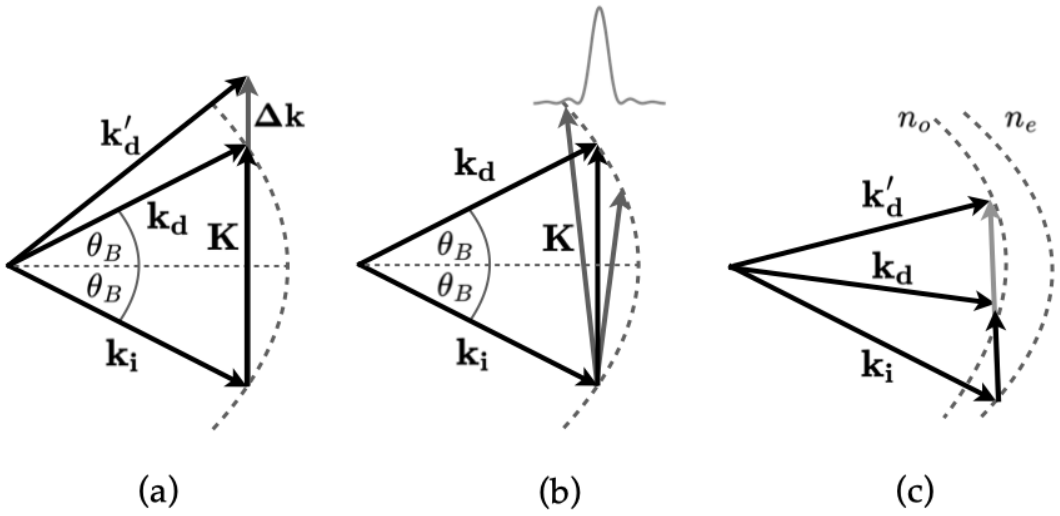


Figure 2.2: (a) Isotropic plane wave interaction, only one frequency exactly obeys phase-matching condition. The diffraction efficiency decreases with increased phase mismatch Δk. (b) Isotropic interaction with finite single-frequency bandwidth determined by transducer lineshape. (c) Anisotropic interaction, with two frequencies exactly obeying phase-matching condition.

2.1.2 Diffraction efficiency

The diffraction efficiency depends on the acoustic wave power P, phase mismatch Δk, and various properties of the acoustic medium. A detailed analysis yields the following expression for the diffraction efficiency [17]:

$$\eta = \kappa \cdot \mathrm{sinc}^2 \frac{1}{\pi} \sqrt{\kappa + \left(\frac{\Delta k L}{2}\right)^2} \tag{2.6}$$

$$\kappa = \left(\frac{\pi^2 M_2 L}{2\lambda^2 H}\right) \cdot P \tag{2.7}$$

where L and H are the acoustic interaction length and beam height, λ is the optical wavelength, and M_2 is the material figure of merit (see Ref. [17]). For $\kappa \ll 1$, the efficiency is approximately linear in acoustic power $\eta \propto P$. At a fixed power, the frequency dependence of diffraction follows a $\mathrm{sinc}^2(\Delta k L/2)$ dependence on the phase mismatch $\Delta k \sim (f - f_0)/v$, where f_0 is the acoustic frequency with exact phase matching and v is the acoustic velocity.

This determines the frequency bandwidth of diffraction.

Moreover, the acoustic waves have an angular spectrum determined by the transducer's aperture, giving a range of acoustic frequencies over which quasi-phase-matching can occur for each drive tone. For typical square tranducers, this angular spectrum follows a $\mathrm{sinc}^2(\pi L f \sin(\theta)/v)$ dependence [18], increasing the angular spread for single-frequency diffraction and thus influencing the resolution of the device (i.e., the number of resolvable spots, a relevant consideration for AOD-generated optical tweezers).

High diffraction efficiency across a large frequency bandwidth is desirable for many acousto-optic applications, notably the generation of large optical tweezer arrays. Increased bandwidth can be achieved by the use of a birefringent acoustic medium, in which the refractive index is anisotropic. As illustrated in Figure 2.2(c), birefringent diffraction occurs between an ordinary and an extraordinary wave, with the acoustic wavevector bridging the corresponding refractive index surfaces. This process requires the incident light to be linearly polarized along a specific axis and results in a 90° rotation of its polarization. In the tangential phase-matching configuration, two distinct acoustic wavevectors exactly satisfy the phase-matching condition, significantly enhancing the device bandwidth. This configuration is widely used in high-bandwidth acousto-optic devices and produces a characteristic double-peaked diffraction efficiency curve, as shown in Figure 2.4(b).

2.2 Intermodulation in acousto-optic devices

Multifrequency acousto-optic diffraction generates intermodulation products at linear combinations of the fundamental driving frequencies. These spurious diffraction products are relevant in neutral atom experiments because tweezer arrays and multi-site addressing beams are generated by driving AODs at multiple frequencies. Intermodulation is a particularly important consideration in local addressing, since the products can coincide with unaddressed sites, leading to crosstalk that limits operation fidelity. The order of an intermodulation

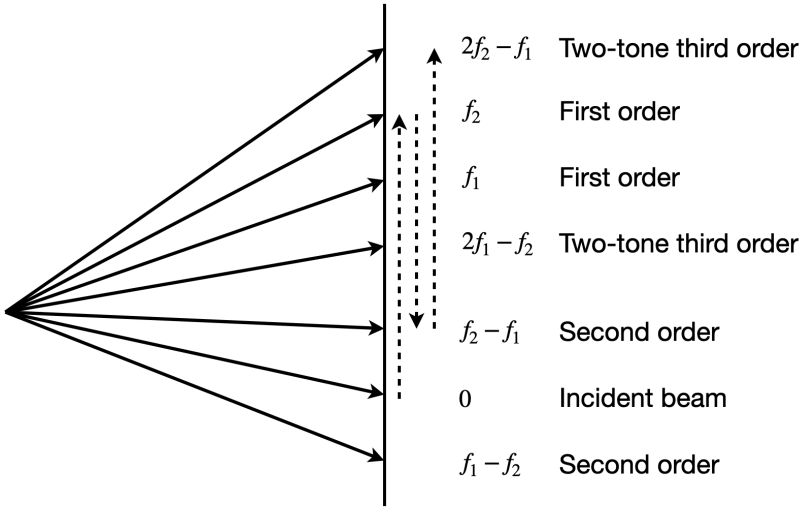


Figure 2.3: Multiple rediffraction for two driving frequencies f_1 and f_2. The dashed lines illustrate the scattering events that produce one of the two-tone third order intermodulation products.

product corresponds to the number of interacting frequencies, or equivalently, the number of terms involved in the frequency combination. The third-order intermodulation products, of the form $\omega_1 \pm \omega_2 \pm \omega_3$, are typically of greatest interest because they lie close to the fundamental frequencies, preventing spatial filtering.

In general, intermodulation in acousto-optic devices arises due to both rediffraction and nonlinearity of the acoustic medium [19].

2.2.1 Rediffraction

Rediffraction is the scattering of light by multiple acoustic phonons, as depicted in Figure 2.3 for the simple case of two frequencies. Ref. [20] derives the efficiency of the two-tone third-order intermodulation products produced by rediffraction in the small-signal limit to be:

$$\eta' = \frac{\eta_1^2 \eta_2}{36} \sim \eta^3 \tag{2.8}$$

where η_i is the efficiency of the two first order tones, and the phase mismatch of the second- and third-order rediffractions is neglected. The cubic dependence of the third-order efficiency on the first-order efficiencies is an intuitive consequence of multiple phonon-photon scattering events, each occurring with efficiency η.

2.2.2 Acoustic nonlinearity

In a nonlinear medium, waves do not obey the principle of linear superposition, leading to the emergence of cross-product terms. As demonstrated by the trigonometric identity:

$$\cos(\omega_1 t)\cos(\omega_2 t) = \frac{1}{2}\big(\cos((\omega_1+\omega_2)t) + \cos((\omega_1-\omega_2)t)\big) \tag{2.9}$$

such nonlinear interactions produce new frequency components at the sum and difference of the original frequencies. The magnitude of this nonlinear interaction varies widely depending on the properties of the acoustic medium (nonlinear acoustic coefficients, acousto-optic figure-of-merit, etc.), optical wavelength, and acoustic frequency/power. However, its role in intermodulation generation in paratellurite (TeO_2) – among the most commonly used acousto-optic materials – is greatly reduced because the third-order elastic constants are identically zero by symmetry, yielding only fourth- and higher-order contributions that are small compared to rediffraction [21].

2.2.3 Experimental characterization in TeO_2 slow-shear mode AOD

The intermodulation products of a 2-axis acousto-optic deflector operating using the TeO_2 slow-shear mode (AA-Opto DTSXY-400-532) were characterized by imaging the first-order diffraction pattern of an incident 497nm laser beam (Vexlum VALO SHG SF) on a high-resolution CMOS camera (BFLY-PGE-13H2M, 1280x960 pixels, pixel size = 3.4 μm). The RF drive for each AOD axis was generated by the DACs on a ZCU216 RFSoC running a modified version of the Fermilab QICK (Quantum Instrumentation Control Kit) firmware

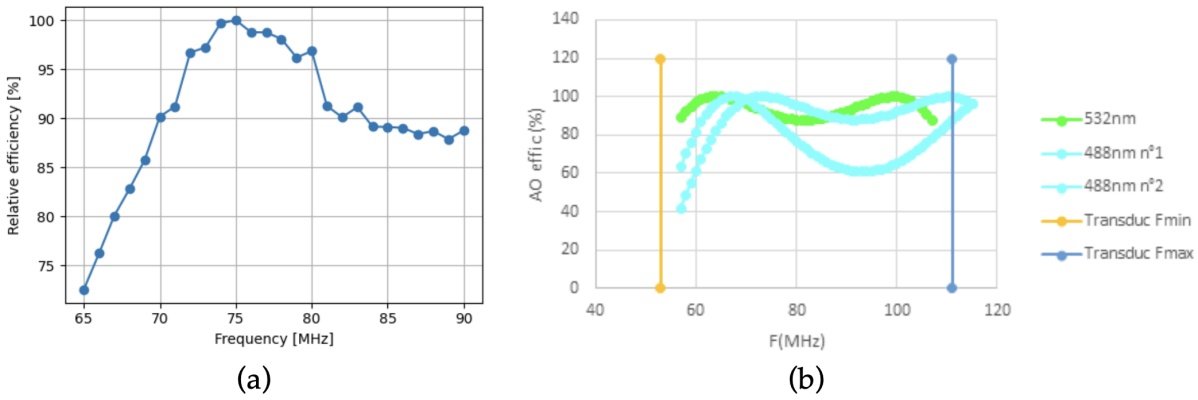


Figure 2.4: (a) Measured DTSXY-400-532 single-axis diffraction efficiency at 497nm (relative to peak efficiency to match the datasheet). (b) Plot provided by AA-Optoelectronics for the DTSXY-400-532 diffraction efficiency. The two blue curves correspond to the 1st and 2nd order efficiencies at 497nm.

[22]. A 30dB amplifier (ZHL-1-2W+) was used to provide the ∼1W of RF power needed to saturate the AOD efficiency, with the RFSoC control software digitally rescaling the amplitude for multi-frequency outputs by $1/\sqrt{N}$ to maintain constant average power for an arbitrary number of frequency components.[1]

AODs operating with the TeO_2 slow-shear mode are used in the main Yb-171 experiment for optical tweezer generation at 487nm, and will be used to perform local addressing at 497nm (see Chapter 3), thus the intermodulation properties are of practical relevance. In particular, we are interested in verifying the η^3 scaling of the third-order intermodulation product efficiency; the ratio of the third-order to first-order powers will consequently scale like η^2, allowing for quadratic suppression of such spurious diffraction products by operating the AOD at a lower diffraction efficiency (and compensating for the decreased first-order output power as needed by increasing the incident laser power).

First, Bragg angle alignment was performed for the horizontal axis of the 2D AOD by maximizing the diffracted first-order power with a power meter. The RF power was

[1]Carefully randomizing the relative phase of the frequency components is important, as constructive interference can produce peak powers higher than the sum of the average power at each frequency, potentially damaging the device.

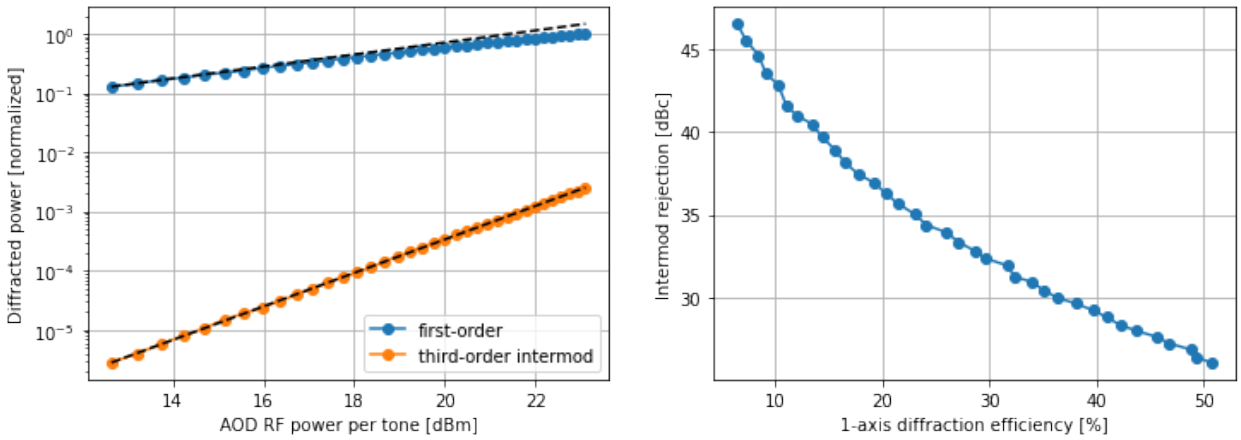


Figure 2.5: The measured first-order and third-order intermodulation powers are plotted on the left, normalized by the maximum measured power. The power law fits are $P_{\text{first-order}} \propto P^{1.01(7)}$ and $P_{\text{intermod}} \propto P^{2.92(2)}$, where the fits are performed in the low power regime to exclude nonlinearity due to efficiency saturation. The intermod rejection $R = 10\log_{10}(P_{\text{first-order}}/P_{\text{intermod}})$ is plotted on the right against the diffraction efficiency.

increased until the first-order power reached saturation, and the diffraction efficiency was measured over the RF frequency range 65-90 MHz, matching the datasheet provided by AA-Optoelectronics, as shown in Figure 2.4.

Next, the two-tone third-order intermodulation product power dependence on diffraction efficiency was measured by driving the horizontal AOD with two frequencies centered around 80 MHz (the middle of the transducer range) and sweeping the RF amplitude to adjust the first-order diffraction efficiency. A 100mm achromatic lens was used to focus the diffracted beam onto the CMOS camera. The images were segmented by detecting the centroids of the bright first-order spots, then calibrating the affine transformation from drive frequency to camera coordinates. Using this method, the two-tone third-order intermodulation products could be reliably located in each image despite their low intensity. The amplitude of the 2D Gaussian fit to a bounding box around each spot was consequently used to determine the spot intensity.

Since the intermodulation power decreases quickly with diffraction efficiency, the dynamic range of the camera was insufficient to measure the amplitude of both the first-order and

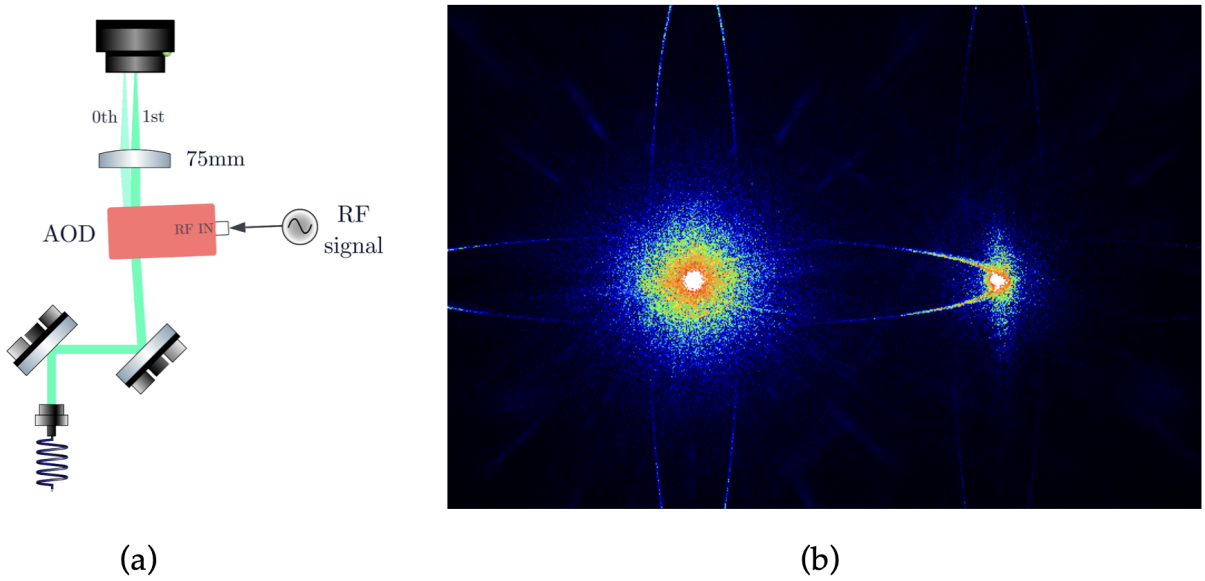
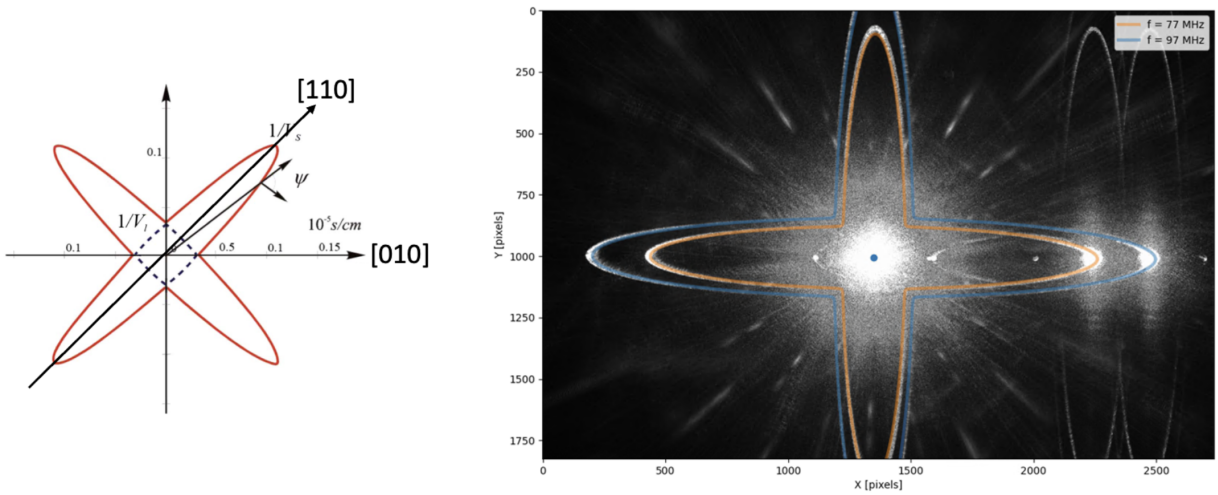


Figure 2.6: (a) Experimental setup for simultaneous imaging of zeroth- and first-order diffracted beams. (b) Unprocessed camera image showing cross-shaped diffraction pattern associated with the acoustic phonon dispersion of the slow-shear mode in paratellurite

third-order spots over a wide range of efficiencies. Two techniques were used to circumvent this limitation: (1) intermodulation products were imaged at higher exposure times than first-order products and the fitted amplitudes were linearly rescaled relative to a reference exposure time, and (2) the incident 497nm laser power was increased significantly to enable measurement of the intermodulation products at low RF drive powers, and ND filters were subsequently added to the imaging path to measure the first-order powers, similarly rescaling the fitted amplitudes by the filter attenuation.

Figure 2.5 shows the measurement of the diffracted first-order powers and two-tone third-order intermodulation product powers as a function of applied RF power. The first-order power scales linearly with the applied RF power in the low-power regime, $P_{\text{first-order}} \propto P_{RF}$, and the intermodulation product power scales like $P_{\text{intermod}} \propto P_{RF}^{2.92}$, approximately matching the expected P^3 dependence. To achieve a rejection $\geq$40dB, the AOD must be operated at a diffraction efficiency $\leq 10\%$.



(a) (b)

Figure 2.7: (a) Plot of acoustic slowness $1/v$ in the (001) plane for the slow-shear mode in paratellurite. The transducer launches acoustic waves at a small angle with the (110) axis, where the acoustic velocity reaches a minimum of 650 m/s. (b) Log-scale image of zeroth- and first-order diffracted beams for two acoustic drive frequencies, 77 and 97 MHz. The predicted diffraction patterns are plotted in blue and orange, showing close agreement with the observed patterns. The second-order intermodulation products are also visible around the zeroth-order beam, illustrating the process of rediffraction.

2.3 Acoustic phonon dispersion

Arc-shaped diffraction patterns were also observed when the first-order diffracted spots were imaged at high exposure in the experimental setup used to study intermodulation power scaling. A short focus lens was used to simultaneously image the zeroth- and first-order beams, revealing that the arcs were connected to a larger cross-shaped diffraction pattern centered on the zeroth-order beam, as shown in Figure 2.6. Upon review of literature focused on the acousto-optic properties of TeO_2, the shape of the diffraction pattern was found to correspond with the inverse acoustic velocity (or "acoustic slowness") for the slow-shear mode of TeO_2 in the plane of optical interaction, i.e. normal to the incidence vector. The following analytic expression for the acoustic velocity of the slow-shear mode in the (001)

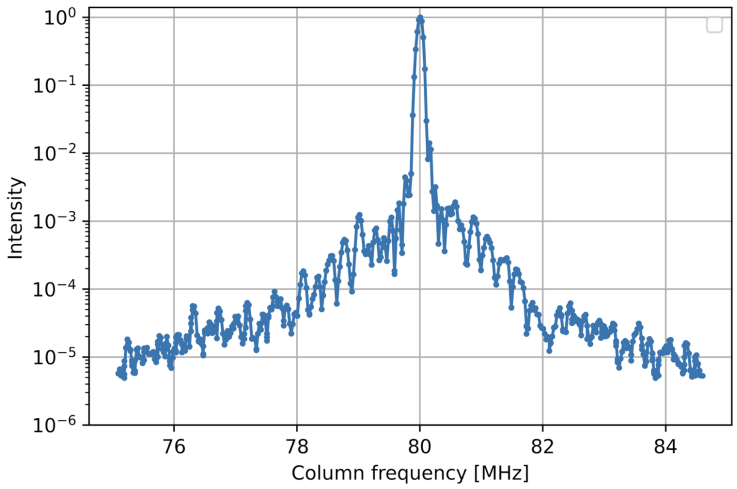


Figure 2.8: Power profile along the acoustic phonon dispersion pattern. The central peak corresponds to the first-order diffraction product, with power decreasing away from the center frequency like $\sim 1/(\Delta f)^2$, consistent with the expected spectral envelope for a square transducer. The spurious power remains greater than -40dB within a $\Delta f = \pm 2$ MHz region around the center frequency.

plane of TeO_2 is provided in Ref. [23] in terms of photo-elastic coefficients c_{ij}:

$$v_{SS}^2(\theta) = \frac{1}{2\rho} \cdot \left((c_{11} + c_{66}) - \sqrt{(c_{66} - c_{11})^2 \cos^2(2\theta) + (c_{12} + c_{66})^2 \sin^2(2\theta)} \right) \tag{2.10}$$

The imaged diffraction pattern can consequently be predicted with no free parameters using Eq. (2.2), making the small-angle approximation $\sin\alpha \approx \alpha$ and expressing the displacement of the diffracted beam from the zeroth-order beam in units of camera pixels as $\alpha d/s$, where d is the focal length of the imaging lens and s is the pixel size. Altogether, this yields the following equation for the diffraction displacement as a function of angle in the imaging plane:

$$r(\theta) = \frac{\lambda f}{2 v_{SS}(\theta)} \cdot \frac{d}{s} \tag{2.11}$$

The predicted and observed diffraction patterns are in close agreement, as shown in Figure 2.7. This indicates that although the transducer primarily launches slow-shear acoustic waves along the (110) axis, there are waves propagating at all angles in the interaction plane as

a result of internal reflection within the crystal. A combination of phase-mismatch (i.e., not connecting the extraordinary and ordinary refractive index surfaces in the wavevector picture) and low power density contribute to the low efficiency of these phonon-photon scattering processes. Since this spurious diffraction pattern results from single phonon-photon scattering events, it scales linearly with the first-order diffracted power, in contrast with intermodulation products produced by multiple scattering events. The power profile of the diffraction pattern was measured, as shown in Figure 2.8. Crosstalk arising from overlap of diffraction arcs with neighboring array sites can be mitigated by avoiding certain frequency spacings in the design of the addressing array. In particular, a spacing of $\Delta f \approx 0.73\,\mathrm{MHz}$ results in arc overlap with nearby sites, with the spurious power exceeding $-40\mathrm{dB}$ relative to the main spot power as determined by the measurement in Figure 2.8, and should therefore be avoided.

Chapter 3

Local Phase Gates with Light Shifts in Yb-171

Phase gates are fundamental single-qubit operations that introduce a relative phase between the computational basis states, enabling rotations about the Z-axis of the Bloch sphere. Mathematically, a general phase gate applies the transformation:

$$|0\rangle \to e^{i\phi_0} |0\rangle \tag{3.1}$$

$$|1\rangle \to e^{i\phi_1} |1\rangle \tag{3.2}$$

where only the relative phase $\phi = \phi_1 - \phi_0$ is physically meaningful. A canonical example is the Pauli Z-gate, which maps $|0\rangle \to |0\rangle$ and $|1\rangle \to -|1\rangle$ up to a global phase. In neutral atom platforms, this operation can be achieved by coupling one or both qubit basis states to an auxiliary excited-state manifold and driving detuned Rabi oscillations that return the population to its initial state. The phase acquired over this round-trip evolution can be interpreted geometrically as the area enclosed by the trajectory on the Bloch sphere. This provides a flexible mechanism for implementing arbitrary $Z(\theta)$ rotations.

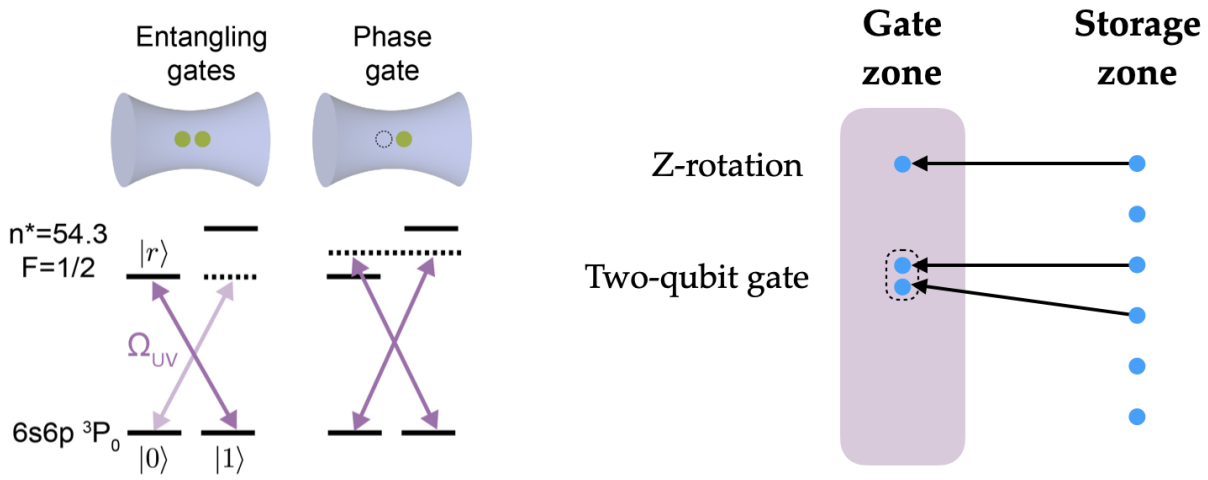


Figure 3.1: Level diagram depicting the current scheme for local phase gates using the 302nm Rydberg transition, and an illustration of local addressing based on atom transport.

3.1 Local Rydberg phase gate

Local single-qubit $Z(\theta)$ rotations can be performed with the 302nm Rydberg laser used for two-qubit entangling gates. Site-selectivity is achieved by atom transport from the "storage zone" into the "gate zone" overlapping the 302nm beam waist, as depicted in Figure 3.1. In the entangling gate scheme, two atoms are brought close together in the gate zone, and the UV frequency is resonant with the Rydberg state transition $|1\rangle \rightarrow |r\rangle$, with the Rydberg blockade preventing double excitation of the $|11\rangle$ state. In the phase gate scheme, a single atom is transported to the gate zone, and the UV frequency is detuned halfway between the two hyperfine Rydberg states $m_F = \pm 1/2$. The $|0\rangle$ and $|1\rangle$ states accumulate equal and opposite phase when undergoing detuned Rabi oscillations, enabling the implementation of arbitrary phase gates.

The main disadvantages of local addressing based on atom transport are slow movement time $\tau_{\text{move}} \sim 1$ ms and errors due to atom loss. This motivates the development of faster, higher-fidelity in situ methods for local addressing of single-qubit phase gates.

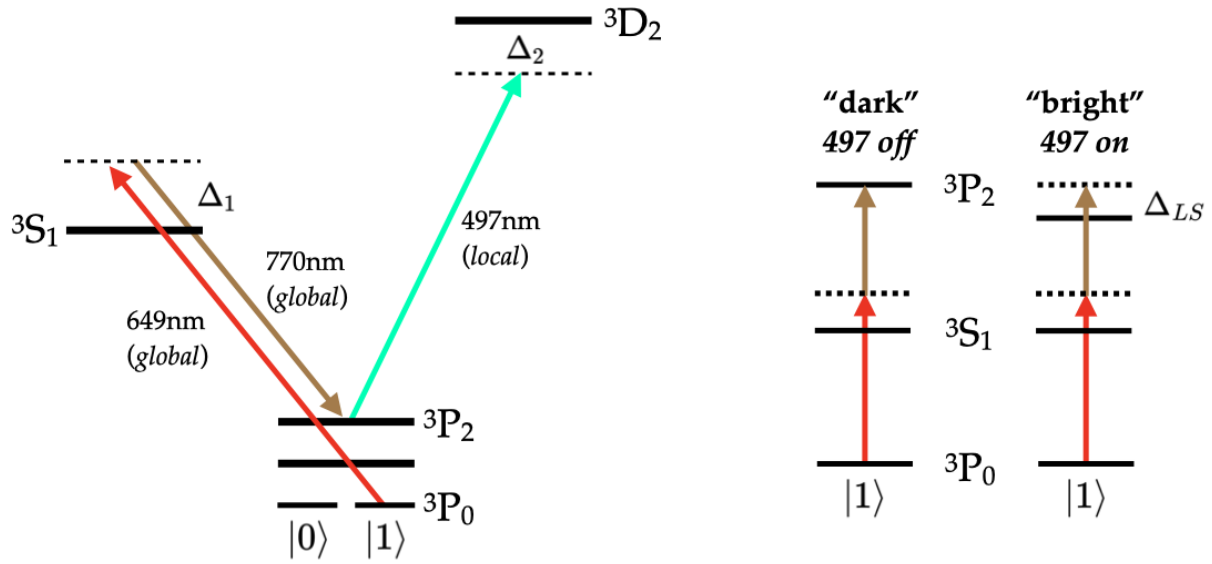


Figure 3.2: Level diagram illustrating the proposed scheme for performing local phase gates, with global 649nm and 770nm beams that drive a Raman transition and local 497nm beams that light-shift the Raman transition out of resonance at selected sites.

3.2 Raman phase gate with local light shifts

Acousto-optic deflectors provide an alternative to physical transport for local addressing by enabling selective illumination of sites directly within the storage zone. While an AOD could be used to locally address the laser driving the phase gate transition, this approach is highly sensitive to power fluctuations from atom displacement relative to the narrow beam waist. To mitigate this, a hybrid scheme is used: a global "gate" laser uniformly illuminates the array, minimizing sensitivity to beam overlap fluctuations, while a second, locally-addressed "control" laser shifts the excited state of the gate out of resonance, effectively disabling the phase gate transition at selected sites. For sufficiently large light shifts, power fluctuations in the control laser will have a small effect on gate fidelity.

3.2.1 Raman transition: $^3\mathbf{P_0} \rightarrow {}^3\mathbf{S_1} \rightarrow {}^3\mathbf{P_2}$

An excited state with a long radiative lifetime is desirable for achieving a high-fidelity phase gate, to mitigate errors induced by excited-state decay. The metastable $6s6p\ ^3P_2$ manifold in ^{171}Yb with lifetime $\tau \sim 15$s (predicted by Ref. [24]) is a suitable candidate, but direct excitation from the $^3P_0$ computational subspace is electric-dipole-forbidden. A two-photon Raman transition through an intermediate state such as $6s7s\ ^3S_1$ provides a dipole-allowed pathway for $^3P_0 \rightarrow {}^3P_2$ Rabi oscillations at convenient optical wavelengths. The effective Rabi frequency for this two-photon transition is:

$$\Omega_R = \frac{\Omega_1 \Omega_2}{2\Delta} \tag{3.3}$$

where Ω_1, Ω_2 are the Rabi frequencies for the 649nm $^3P_0 \rightarrow {}^3S_1$ and 770nm $^3S_1 \rightarrow {}^3P_2$ transitions and Δ is the intermediate state detuning.

There are several considerations in designing a high-fidelity gate using this transition.

(1) Since $^3P_2$ is anti-trapped by the 487nm tweezers, the gate must be performed within the trap-off time of the 1MHz trap modulation cycle in order to prevent atom loss, giving a target gate time $\tau_g \leq 1\mu$s.

(2) Due to the short lifetime of the $^3S_1$ state ($\tau \sim 15.9$ns measured by Ref. [25]), the intermediate-state detuning Δ must be much larger than the single-photon Rabi frequency Ω to suppress scattering into $^3S_1$, as this population would rapidly decay and introduce gate errors. The far-detuned scattering rate to an excited state with linewidth Γ is given by:

$$\tilde{\Gamma} \approx \frac{\Omega^2}{4\Delta^2}\Gamma \quad (\Delta \gg \Omega, \Gamma) \tag{3.4}$$

The total scattering error over a gate with duration τ_g is approximately given by $\epsilon_c \sim \tilde{\Gamma}\tau_g$. Assuming for simplicity that the 649nm and 770nm Rabi frequencies are equal $\Omega_1 = \Omega_2 = \Omega$, the Raman Rabi frequency is $\Omega_R = \Omega^2/(2\Delta) = 2\pi/\tau_g$. Substitution into Eq. (3.4) yields

the following expression for scattering error in terms of the intermediate-state detuning and linewidth:

$$\epsilon_{\text{sc}} \propto \frac{\Gamma}{\Delta} \tag{3.5}$$

Thus to achieve gate scattering error $\epsilon_{\text{sc}} \sim 10^{-4}$, the intermediate-state detuning must be $\Delta \sim 2\pi \times 100$ GHz, given the measured $^3S_1$ linewidth $\Gamma = 2\pi \times 10$ MHz [25]. For the target gate time $\tau_g = 1\mu$s, this requires the single-photon Rabi frequencies to be of order $\Omega = \sqrt{2\Omega_R\Delta} \sim 2\pi \times 500$ MHz.

(3) The differential light shift induced by the 649nm beam on the $|0\rangle$ and $|1\rangle$ states should be minimal to avoid dephasing of unaddressed sites. This rules out the use of pure σ^+/σ^- transitions, as the matrix elements differ for the $|0\rangle \equiv |^3P_0, m_F = -1/2\rangle \rightarrow |^3S_1, F = 3/2, m_F = -1/2 \pm 1\rangle$ and $|1\rangle \equiv |^3P_0, m_F = 1/2\rangle \rightarrow |^3S_1, F = 3/2, m_F = 1/2 \pm 1\rangle$ transitions. This differential light shift can be mitigated by driving the 649nm transition with either π-polarization or an equal mixture of circular polarizations σ^+ and σ^-, ensuring the light shifts on $|0\rangle$ and $|1\rangle$ are equal up to small differences in intermediate-state detuning caused by Zeeman splitting of the m_F sublevels of $|^3S_1\rangle$. Note that it is preferable to use the σ^+ transitions because their matrix elements are larger, easing laser power requirements, and because intermediate-state-mediated bit flips from $|1\rangle \rightarrow |0\rangle$ are forbidden by selection rules.

(4) Population transfer from $|0\rangle \rightarrow |^3P_2\rangle$ should be minimized. While a scheme similar to the Rydberg phase gate could be used, in which the Raman transition frequency is detuned halfway between two $^3P_2$ sublevels and the $|0\rangle$ and $|1\rangle$ states accumulate equal and opposite phase, this would require larger light shifts to suppress for local addressing. Thus we restrict our focus to near-resonant Rabi oscillations between $|1\rangle \rightarrow |^3P_2, F = 5/2\rangle$. The Zeeman splitting between adjacent m_F sublevels in the $|^3P_2, F = 5/2\rangle$ manifold is 1.68 MHz/G, giving a splitting of $\delta = 8.4$ MHz for the $B = 5G$ field used in the current experiment. For σ^+-polarized 649nm and 770nm drives, Clebsch-Gordan coefficients suppress the Raman Rabi frequency for the $|0\rangle \rightarrow |^3P_2, F = 5/2, m_F = 3/2\rangle$ transition by a factor of $\sqrt{1/5}$ compared

to the $|1\rangle \rightarrow |^3P_2, F = 5/2, m_F = 5/2\rangle$ transition. Assuming a gate Rabi frequency $\Omega_R = 2\pi \times 1$ MHz, this yields the following gate error due to $|0\rangle \rightarrow |^3P_2\rangle$ population transfer:

$$\epsilon_{\text{pop}} \sim \Pr(0 \rightarrow {}^3P_2) \sim \frac{(\Omega_R/\sqrt{5})^2}{\delta^2} \approx 2 \times 10^{-3} \tag{3.6}$$

This error increases when driving with π-polarization, as $|0\rangle$ population transfer is suppressed only by the Zeeman splitting. Thus either adiabatic gate shaping to ensure population return to $|0\rangle$, or a larger magnetic field $B \sim 25G$ will be necessary to achieve lower gate error $\epsilon_{\text{pop}} \sim 10^{-4}$.

3.2.2 Light shifts: $^3P_2 \rightarrow {}^3D_2$

Site selectivity in the Raman phase gate scheme can be realized through the use of an AOD to locally address light shifts on the $^3P_2$ state, detuning it far out of resonance with the Raman transition. The 497nm transition $^3P_2 \rightarrow 6s6d\ ^3D_2$ is a suitable choice for inducing this shift, as selection rules prevent any scattered population from decaying into the $^3P_0$ computational subspace. In the following, we adapt an analysis from Ref. [26] to determine the required parameters to achieve a target gate fidelity. We assume for simplicity that the Raman transition drives on-resonant Rabi oscillations with Rabi frequency Ω_g between $|1\rangle$ and $|^3P_2, F = 5/2, m_F = 5/2\rangle$ to implement a Z-gate.

The π-transition $|^3P_2, F = 5/2, m_F = 5/2\rangle \rightarrow |^3D_2, F = 5/2, m_F = 5/2\rangle$ has the largest matrix element $\langle \mathbf{d} \rangle = 0.58 \cdot e a_0$, and thus the lowest 497nm power requirements. The light shift on $|^3P_2, F = 5/2, m_F = 5/2\rangle$ produced by driving this transition at 497nm with Rabi frequency Ω_c and detuning Δ is:

$$\Delta_{LS} = \frac{\Omega_c^2}{4\Delta} \tag{3.7}$$

The "rotation" error caused by residual Raman excitation from $|1\rangle \rightarrow |^3P_2\rangle$ in the presence

of this light shift is given by:

$$\epsilon_{\text{rot}} = \Pr(|1\rangle \to |^3P_2\rangle) \tag{3.8}$$

$$= \frac{\Omega_g^2}{\Delta_{LS}^2} = \frac{16\Omega_g^2\Delta^2}{\Omega_c^4} \tag{3.9}$$

while the error due to scattering from $|^3P_2\rangle \to |^3D_2\rangle$ is given by:

$$\epsilon_{\text{sc}} = \frac{\tilde{\Gamma}}{2\pi} \cdot \tau_g \cdot \Pr(|1\rangle \to |^3P_2\rangle) \tag{3.10}$$

where $\tilde{\Gamma}$ is the detuned scattering rate given by Eq. (3.4) and $\tau_g = 2\pi/\Omega_g$ is the gate duration. Expanding this expression yields:

$$\epsilon_{\text{sc}} = \frac{\Omega_c^2}{4\Delta^2}\frac{\Gamma}{2\pi} \cdot \frac{2\pi}{\Omega_g} \cdot \frac{\Omega_g^2}{\Delta_{\text{LS}}^2} \tag{3.11}$$

$$= \frac{4\Omega_g\Gamma}{\Omega_c^2} \tag{3.12}$$

$$= \sqrt{\epsilon_{\text{rot}}} \cdot \frac{\Gamma}{\Delta} \tag{3.13}$$

For a target error rate $\epsilon = \epsilon_{\text{rot}} = \epsilon_{\text{sc}}$, we obtain the following expressions for the control Rabi frequency and detuning:

$$\Omega_c = \sqrt{\frac{4\Omega_g\Gamma}{\epsilon}} \tag{3.14}$$

$$\Delta = \frac{\Gamma}{\sqrt{\epsilon}} \tag{3.15}$$

From Ref. [25], the $^3D_2$ linewidth is $\Gamma = 2\pi \times 6.58$ MHz. Thus for the target error rate $\epsilon = 10^{-4}$ and gate Rabi frequency $\Omega_g = 2\pi \times 1$ MHz, the required 497nm detuning and Rabi

frequency is:

$$\Omega_c = 2\pi \times 515 \text{ MHz} \tag{3.16}$$

$$\Delta = 2\pi \times 660 \text{ MHz} \tag{3.17}$$

$$\Rightarrow \Delta_{LS} = 2\pi \times 100 \text{ MHz} \tag{3.18}$$

Assuming that the addressing beam is focused to a diffraction-limited beam waist $w_0 \approx$ 500 nm, the Rabi frequency as a function of 497nm power can be calculated for the maximal transition matrix element $\langle \mathbf{d} \rangle = 0.58 \cdot e a_0$ using:

$$\Omega = \left| \frac{E_0 \langle \mathbf{d} \rangle}{\hbar} \right| \tag{3.19}$$

$$E_0 = \sqrt{\frac{2I}{\epsilon_0 c}} \tag{3.20}$$

$$I = \frac{2P}{\pi w_0^2} \quad \text{(Gaussian beam)} \tag{3.21}$$

$$\Rightarrow \Omega_c = 2\pi \times 325 \text{ MHz} \times \sqrt{\frac{P}{1\mu\text{W}}} \tag{3.22}$$

Thus achieving the desired Rabi frequency $\Omega_c = 2\pi \times 515$ MHz requires only 2.5 μW of power per site. Note that operating the AOD at $\sim 10\%$ diffraction efficiency in order to achieve 40dB intermod rejection increases this power requirement to 25 μW per site

3.2.3 Master equation simulations

First, numerical simulations of the Lindblad master equation were performed in QuTiP to investigate the effect of intermodulation on Z-gate fidelity. A simple three-level system $|0\rangle$, $|1\rangle$, and $|e\rangle \leftrightarrow |^3P_2\rangle$ with Hamiltonian:

$$\hat{H} = \frac{\Omega}{2}(|e\rangle\langle 1| + |1\rangle\langle e|) - \Delta\,|e\rangle\langle e| \tag{3.23}$$

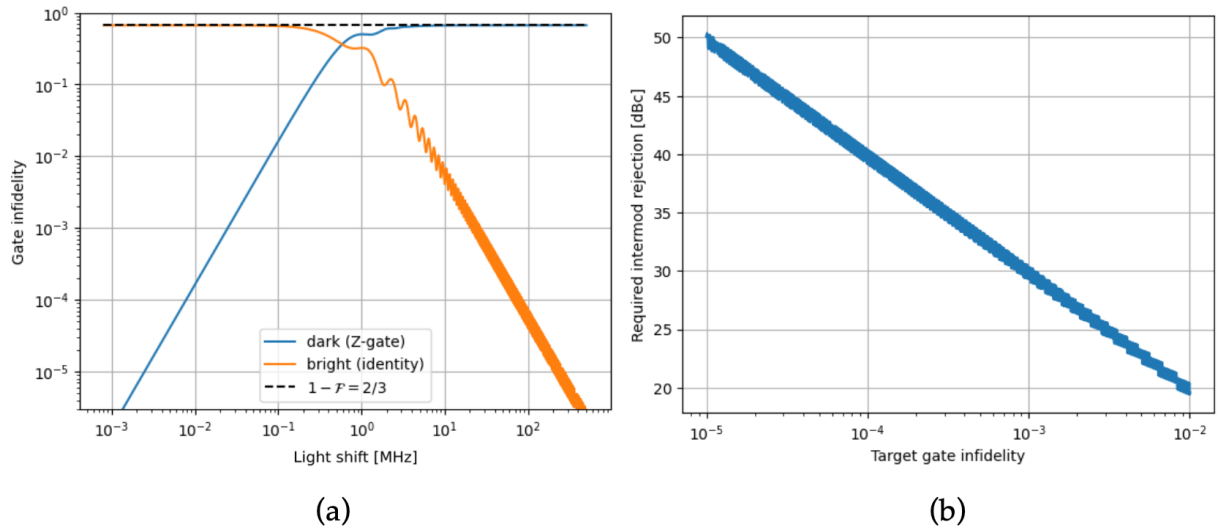


Figure 3.3: (a) Simulated gate infidelity $1 - \bar{F}$ for addressed ("bright") and unaddressed ("dark") sites as a function of the light shift on the Raman transition. (b) Ratio of intermodulation power to first-order power in dBc required to achieve a target gate infidelity, determined by equating the dark and bright infidelities and calculating the ratio between the respective light shifts.

was used to simulate detuned Rabi oscillations between $|1\rangle \rightarrow |e\rangle$, where the detuning Δ models the light shift on $|^3P_2\rangle$ used to achieve local addressing. The system was evolved for time $\tau_g = 2\pi/\Omega$ using the target gate Rabi frequency $\Omega = 2\pi \times 1$ MHz, such that $|1\rangle \rightarrow -|1\rangle$ for $\Delta = 0$, implementing a Z-gate. The average gate fidelity was computed by simulating the evolution of the density matrix basis states in the computational subspace $\{|0\rangle, |1\rangle\}$, reconstructing the superoperator χ_{sim} in the Choi representation, and computing the process fidelity F_p and average gate fidelity $\bar{F}$ using:

$$F_p = \frac{\text{Tr}(\chi_{\text{ideal}}^{\dagger} \cdot \chi_{\text{sim}})}{d^2} \tag{3.24}$$

$$\bar{F} = \frac{dF_p + 1}{d + 1} \tag{3.25}$$

where $d = 2$ is the Hilbert space dimension and χ_{ideal} is the superoperator representation of the ideal gate operation. The dynamics were simulated over a range of detunings Δ and the average gate fidelity was computed for both the ideal Z-gate $\chi_{\text{ideal}} = \sigma_z \otimes \sigma_z$ and the identity

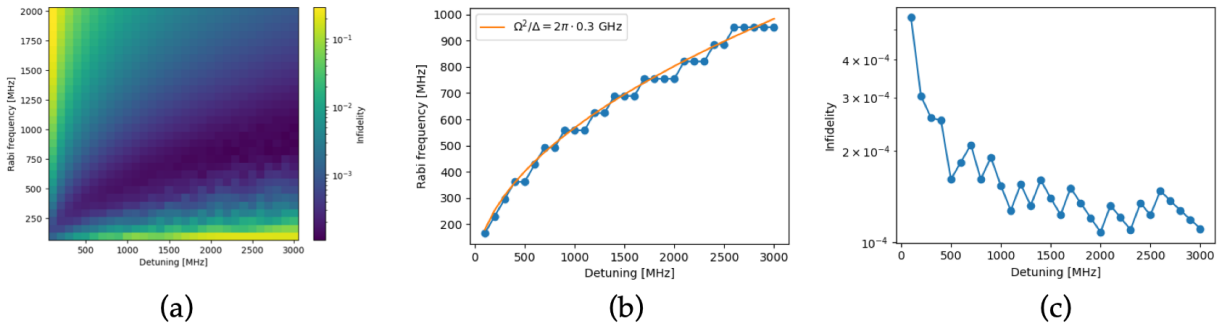


Figure 3.4: (a) Average of the simulated gate infidelities $1-\bar{F}$ for addressed and unaddressed sites, using an intermodulation rejection ratio $r = 10^{-4}$. The infidelity increases when using large Rabi frequencies due to intermodulation, and when using large detunings due to smaller resulting light shifts. (b) Minimal gate infidelity curve for the 2D parameter sweep, compared with the curve of constant light shift $\Delta_{LS} = \Omega^2/4\Delta \sim 2\pi \times 75$ MHz. (c) Average gate infidelity along the minimal curve, plotted as a function of detuning.

operation $\chi_{\text{ideal}} = \mathbb{I} \otimes \mathbb{I}$, respectively modeling the gate fidelity for both the unaddressed sites (with diminishing light shifts) and addressed sites (with large light shifts). Due to intermodulation in the AOD system, unaddressed sites experience residual illumination. Specifically, the resulting light shift is proportional to the intensity of the addressing 497nm laser:

$$\Delta_{LS} = \frac{\Omega_{\text{addr}}^2}{4\Delta_{\text{addr}}} \propto I_{\text{addr}} \tag{3.26}$$

As a result, the ratio of light shifts between unaddressed and addressed sites is equal to the power ratio of the intermodulation products to the first order products. The simulation results are presented in Figure 3.3, showing that the gate infidelity for addressed and unaddressed sites directly corresponds to the intermodulation rejection ratio, $1 - \bar{F} \sim P_{\text{intermod}}/P_{\text{first order}}$.

Next, since the values for Ω_c and Δ that were analytically derived in the previous section to achieve gate error $\epsilon = 10^{-4}$ violate the far-detuned approximation $\Delta \gg \Omega$ made in the light shift calculation, numerical simulations of the Lindblad master equation including the $^3P_2 \rightarrow {}^3D_2$ transition were performed in QuTiP to verify the result. The system was modeled with five levels: $|0\rangle$, $|1\rangle$, $|e\rangle \leftrightarrow |^3P_2\rangle$, $|f\rangle \leftrightarrow |^3D_2\rangle$ and a "dump" level $|d\rangle$ to model decay

from $|^3D_2\rangle$. The system Hamiltonian was:

$$\hat{H} = \frac{\Omega_g}{2}(|1\rangle\langle e| + |e\rangle\langle 1|) + \frac{\Omega_c}{2}(|e\rangle\langle f| + |f\rangle\langle e|) - \Delta\,|f\rangle\langle f| \tag{3.27}$$

with the collapse operator for $|^3D_2\rangle$ decay given by:

$$\hat{c} = \sqrt{\Gamma}\,|d\rangle\langle f| \tag{3.28}$$

where Γ is the $^3D_2$ linewidth. The system was evolved for a duration $\tau = 2\pi/\Omega_g$ with $\Omega_g = 2\pi \times 1$ MHz, as in the previous simulation. The gate fidelity computation was modified to account for leakage error, following Ref. [27]:

$$L = 1 - \frac{\mathrm{Tr}(\mathcal{E}(\mathbb{I}))}{d} \tag{3.29}$$

$$\bar{F} = \frac{dF_p + 1 - L}{d+1} \tag{3.30}$$

where $d = 2$ and $\mathcal{E}$ is the quantum channel represented by the superoperator χ_{sim}. The detuning Δ and control Rabi frequency Ω_c were varied, and the gate fidelity with the identity operation was computed for each parameter combination. To include the effect of intermodulation, the gate fidelity with the ideal Z-gate was also computed for a simulation using Rabi frequency $\Omega_c' = \sqrt{r}\Omega_c$, where r is the power ratio of the intermodulation products and first-order products. Figure 3.4 shows the results for a fixed intermodulation ratio of $r = 10^{-4}$. The optimal average fidelity across addressed and unaddressed sites converges to $1 - \bar{F} = 10^{-4}$, achieved with a roughly constant addressing light shift of $\Delta_{LS} \approx 2\pi \times 75$ MHz. This result is in agreement with the previous analytical method, as an average gate error $1 - \bar{F} \sim 2 \times 10^{-4}$ can be achieved using $\Omega_c \sim 2\pi \times 600$ MHz and $\Delta \sim 2\pi \times 450$ MHz; in fact, the simulation indicates these parameters can be decreased further (keeping the light shift constant) without significant detriment to gate fidelity.

3.3 497nm laser system

The 497nm system is dual-purpose: off-resonant locally-addressed light shifts on $^3P_2$ for performing local phase gates, and on-resonant depumping from $^3P_2$ to remove any anti-trapped population during qubit initialization and readout. Though a complete discussion on depumping is beyond the scope of this thesis, the requirement for both on- and off-resonant 497nm light is an important consideration in the laser system design.[1]

3.3.1 AOM and fiber coupling setup

The depumping process requires two frequencies to drive the $F = 5/2 \rightarrow 5/2$ and $F = 3/2 \rightarrow 3/2$ transitions between the $^3P_2$ and $^3D_2$ states, as all population in $^3P_2$ must be removed to avoid atom loss. The hyperfine constants A_{hf} for each manifold were found in literature and the splitting between the $F = 5/2$ and $F = 3/2$ hyperfine levels were calculated using Equation (3.31), as summarized in Table 3.1.

$$\Delta E_{\text{hf}} = \frac{1}{2} \cdot \big(F(F+1) - I(I+1) - J(J+1)\big) \cdot A_{\text{hf}} \tag{3.31}$$

Level	A_{hf} (MHz)	5/2 – 3/2 Splitting (MHz)	Reference
$6s6p\ ^3P_2$	2677.6	6694.0	[24]
$6s6d\ ^3D_2$	2635(15)	6588(38)	[28]

Table 3.1: Hyperfine constants and splittings for $^3P_2$ and $^3D_2$ states.

The predicted 106(38) MHz frequency difference between the $F = 5/2 \rightarrow 5/2$ and $F = 3/2 \rightarrow 3/2$ transitions is within the range of an AOM, enabling us to avoid the power limitations associated with EOMs. In addition, the results from Section 3.2 indicate that

[1] In the present system, $^3P_2$ depumping is achieved using a 770nm laser addressing the $^3P_2 \rightarrow {}^3S_1$ transition, as described in Chapter 1; this is not optimal, however, given that a small proportion of the $^3S_1$ population decays to the $^3P_0$ subspace, inducing computational errors. Depumping $^3P_2$ through $^3D_2$ avoids this issue, as selection rules prevent decay back to $^3P_0$.

detuning the addressing beam by ∼500 MHz produces sufficient light shifts on $^3P_2$ to achieve 10^{-4} gate infidelity, allowing all necessary frequency-shifting to be performed using AOMs.

Figure 3.5 shows the experimental setup used to frequency shift and fiber couple 497nm light for depumping, local addressing, and frequency stabilization. The 497nm source (Vexlum VALO SHG SF) output was collimated to a 1.7mm beam waist, and a 3:1 telescope was used to reduce the beam waist to ∼0.6mm, as recommended by the AOM (Brimrose TEF-110-40-400/900) datasheet for optimal diffraction efficiency. The depumping and addressing AOMs were aligned to diffract to the +1 and −1 orders respectively in a double-pass configuration. This configuration doubles the frequency shift of the diffracted order, enabling a total frequency separation of approximately $4 \cdot f_{\text{center}} = 440$ MHz between the depumping and addressing beams, with an additional ∼80 MHz shift added through the local addressing AOD.[2] The sidebands used to drive the two depumping transitions were produced by driving the depumping AOM at two frequencies f_0 and f_1 such that $f_1 - f_0 = f_{\text{splitting}}/2$, and a 50mm lens was added prior to retro-reflection to ensure the two sidebands coincided after a double pass and maintained high second-pass diffraction efficiency. The double-pass efficiency was measured to be 24% at $f_0 = 75$ MHz and 37% at $f_1 = 130$ MHz, consistent with the expected relation $\eta_{\text{double}} = \eta_{\text{single}}^2$ and the diffraction efficiency curve $\eta_{\text{single}}(f)$ provided in the AOM datasheet. Simultaneous fiber coupling efficiencies were 43% and 57% for f_0 and f_1, respectively, primarily limited by alignment imperfections in the cat-eye lens system used to ensure beam overlap. With more than 2W of available 497nm power, the measured efficiencies were sufficient to meet the expected ∼10mW depumping power requirement. The frequency separation and relative power of the sidebands after fiber coupling was verified by determining the amplitude and frequency of the beat note measured on a photodiode; this measurement revealed the presence of second-order diffracted light, constituting up to 30% of the total coupled power, but this should not pose significant issues for depumping. At 110MHz, the addressing double-pass and fiber-coupling efficiencies were measured to be 72%

[2] An additional benefit of the double-pass configuration is an improved on/off extinction ratio.

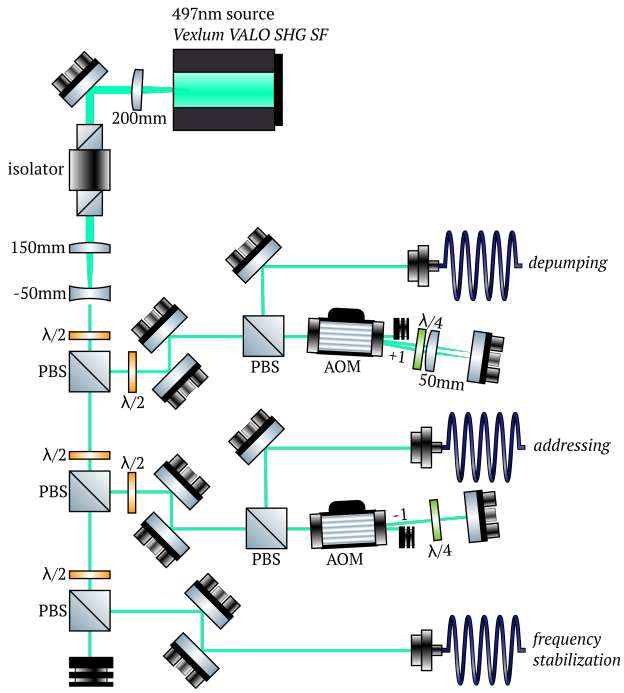


Figure 3.5: Diagram of the experimental setup for frequency-shifting and fiber-coupling 497nm light for local addressing, depumping, and frequency stabilization.

and 60%, respectively — significantly higher than the depumping efficiencies, due to the use of a single frequency at the optimal AOM diffraction point.

Frequency stabilization was performed with a PID feedback loop using the frequency readout of a wavemeter (HighFinesse WS7). The setpoint of this PID controller was proportionally adjusted to track variations in the wavemeter frequency reading of a ULE cavity-stabilized laser at 556nm, compensating for slow wavemeter drifts. Upon installation of a new ULE cavity, this "transfer" lock will be replaced by a direct PDH lock using the 497nm fundamental at 994nm.

3.3.2 Local addressing setup

Due to space constraints on the breadboard for generating the AOD and SLM traps, the setup for launching the local addressing beam was built on a platform raised above the

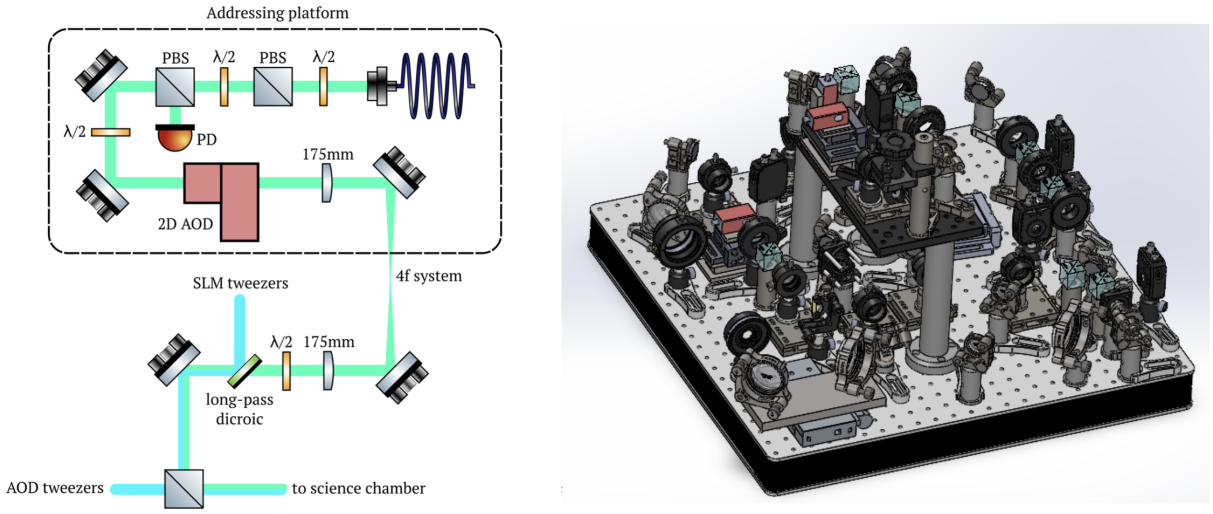


Figure 3.6: Diagram of the local addressing breadboard and combination pathway with AOD/SLM tweezers, and a CAD model of the entire tweezer + addressing setup.

main breadboard. A CAD model of the existing breadboard was developed to identify a non-obstructive location for platform placement and to model the addressing beam path. A 175mm 4f-system was used to coincide the image plane of the addressing AOD with that of the AOD tweezers, ensuring the addressing beam filled the objective without clipping. A long-pass dichroic (AVR Optics DI03-R488-T3-25.4-D) was chosen to combine the SLM tweezers with the the addressing beam. This configuration is advantageous because dichroic wavefront error is typically much higher in reflection than transmission; such distortion can easily be corrected with Zernike polynomials in an SLM, but is difficult to mitigate using an AOD. The dichroic surface flatness was measured using an interferometer to be $\sim \lambda/8$ in reflection at 487nm. The transmission at 497nm and reflection at 487nm were measured as a function of angle-of-incidence: the transmitted 497nm power increased from 0% at 45° to 95% at 52° AOI, and the reflected 487nm power was $\sim$ 100% up to 57° AOI, matching the manufacturer specifications. Given that the scan angle for the AOD is 2.3°, an AOI of 52° will optimally transmit 497nm power across the AOD's usable frequency bandwidth.

3.3.3 Future steps

With the addressing setup now assembled, the next step is integration with the existing breadboard used for AOD and SLM-based tweezer generation. This will involve: (1) rerouting the SLM beam path to combine with the 497nm beam via a long-pass dichroic, (2) adjusting the addressing 4f telescope to align the addressing beam's focal plane with the trap plane—compensating for chromatic focal shifts of the objective, and (3) aligning the addressing AOD to ensure the orientation of the addressing array matches that of the AOD-generated traps.

Implementation of local phase gates will proceed in stages: first by calibrating Raman Rabi oscillations using the 649nm and 770nm beams; then by verifying light shift performance with the global 497nm depumping beam; and finally by incorporating local light shifts using the addressing 497nm system. Fidelity at each stage will be characterized via randomized benchmarking.

In sum, this thesis demonstrated that AOD intermodulation can be mitigated to enable low-crosstalk local addressing, established key requirements for implementing Raman-based phase gates and light shifts, and detailed the construction of the 497nm laser system for future experimental use.

Bibliography

[1] F. Scazza. *Probing SU(N)-Symmetric Orbital Interactions with Ytterbium Fermi Gases in Optical Lattices*. PhD thesis, Ludwig-Maximilians-Universität München, Faculty of Physics, 2015.

[2] S. Ma, G. Liu, P. Peng, B. Zhang, S. Jandura, J. Claes, A. P. Burgers, G. Pupillo, S. Puri, and J. D. Thompson. High-fidelity gates and mid-circuit erasure conversion in an atomic qubit. *Nature*, 622:279–284, 2023. Published: 11 October 2023.

[3] H. Levine, A. Keesling, G. Semeghini, A. Omran, T. T. Wang, S. Ebadi, H. Bernien, M. Greiner, V. Vuletić, H. Pichler, and M. D. Lukin. Parallel implementation of high-fidelity multiqubit gates with neutral atoms. *Physical Review Letters*, 123(17):170503, Oct 2019.

[4] D. Bluvstein, H. Levine, G. Semeghini, T. T. Wang, S. Ebadi, M. Kalinowski, A. Keesling, N. Maskara, H. Pichler, M. Greiner, V. Vuletić, and M. D. Lukin. A quantum processor based on coherent transport of entangled atom arrays. *Nature*, 604:451–456, 2022.

[5] D. Bluvstein, S. J. Evered, A. A. Geim, et al. Logical quantum processor based on reconfigurable atom arrays. *Nature*, 626:58–65, 2024.

[6] N. Schlosser, G. Reymond, I. Protsenko, and P. Grangier. Sub-poissonian loading of single atoms in a microscopic dipole trap. *Nature*, 411(6841):1024–1027, 2001.

[7] H. J. Manetsch, G. Nomura, E. Bataille, K. H. Leung, X. Lv, and M. Endres. A tweezer array with 6100 highly coherent atomic qubits. arXiv preprint 2403.12021, March 2024.

[8] M. Saffman, T. G. Walker, and K. Mølmer. Quantum information with Rydberg atoms. *Reviews of Modern Physics*, 82:2313–2363, Sep 2010.

[9] D. Jaksch, J. I. Cirac, P. Zoller, S. L. Rolston, R. Côté, and M. D. Lukin. Fast quantum gates for neutral atoms. *Physical Review Letters*, 85(10):2208–2211, 2000.

[10] M. Norcia, A. Young, and A. Kaufman. Microscopic control and detection of ultracold strontium in optical-tweezer arrays. *Physical Review X*, 8:041054, 2018.

[11] A. Cooper, J. P. Covey, I. S. Madjarov, S. G. Porsev, M. S. Safronova, and M. Endres. Alkaline-earth atoms in optical tweezers. *Physical Review X*, 8:041055, 2018.

[12] S. Saskin, J. T. Wilson, B. Grinkemeyer, and J. D. Thompson. Narrow-line cooling and imaging of ytterbium atoms in an optical tweezer array. *Physical Review Letters*, 122:143002, 2019.

[13] A. J. Daley, M. M. Boyd, J. Ye, and P. Zoller. Quantum computing with Alkaline-Earth-Metal atoms. *Physical Review Letters*, 101(17):170504, Oct 2008.

[14] I. S. Madjarov, J. P. Covey, A. L. Shaw, J. Choi, A. Kale, A. Cooper, H. Pichler, V. Schkolnik, J. R. Williams, and M. Endres. High-fidelity entanglement and detection of alkaline-earth rydberg atoms. *Nature Physics*, 16:857–861, 2020.

[15] Y. Wu, S. Kolkowitz, S. Puri, and J. D. Thompson. Erasure conversion for fault-tolerant quantum computing in alkaline earth rydberg atom arrays. *Nature Communications*, 13:4657, 2022.

[16] A. Korpel. Acousto-optics — a review of fundamentals. *Proceedings of the IEEE*, 69(1):48–53, 1981.

[17] I. C. Chang. *Acousto-Optic Devices and Applications*, volume 2, pages 12–1–12–30. McGraw-Hill, 1995.

[18] I. Peled, R. Kaminsky, and Z. Kotler. Acousto-optics bandwidth broadening in a bragg cell based on arbitrary synthesized signal methods. *Applied Optics*, 54:5065–5073, 2015.

[19] G. Elston. Intermodulation products in acousto-optic signal processing systems. *IEEE 1985 Ultrasonics Symposium*, pages 391–397, 1985.

[20] D. L. Hecht. Multifrequency acoustooptic diffraction. *IEEE Transactions on Sonics and Ultrasonics*, 24(1):7–18, January 1977.

[21] M. G. Gazalet, J. C. Kastelik, C. Bruneel, O. Bazzi, and E. Bridoux. Acousto-optic multifrequency modulators: reduction of the phase-grating intermodulation products. *Applied Optics*, 32:2455–2460, 1993.

[22] L. Stefanazzi, K. Treptow, N. Wilcer, C. Stoughton, C. Bradford, S. Uemura, S. Zorzetti, S. Montella, G. Cancelo, S. Sussman, A. Houck, S. Saxena, H. Arnaldi, A. Agrawal, H. Zhang, C. Ding, and D. I. Schuster. The QICK (quantum instrumentation control kit): Readout and control for qubits and detectors. *Review of Scientific Instruments*, 93(4):044709, 2022.

[23] V. Voloshinov, N. Polikarpova, P. Ivanova, and V. Khorkin. Acousto-optic control of internal acoustic reflection in tellurium dioxide crystal in case of strong elastic energy walkoff. *Applied Optics*, 57(10):C19–C25, 2018.

[24] S. G. Porsev, Y. G. Rakhlina, and M. G. Kozlov. Electric-dipole amplitudes, lifetimes, and polarizabilities of the low-lying levels of atomic ytterbium. *Physical Review A*, 60(4):2781–2785, Oct 1999.

[25] M. Baumann, M. Braun, A. Gaiser, and H. Liening. Radiative lifetimes and g_j factors of low-lying even-parity levels in the Yb I spectrum. *Journal of Physics B: Atomic, Molecular and Optical Physics*, 18:L601–L605, 1985.

[26] A. P. Burgers, S. Ma, S. Saskin, J. Wilson, M. A. Alarcón, C. H. Greene, and J. D. Thompson. Controlling Rydberg excitations using ion-core transitions in alkaline-earth atom-tweezer arrays. *PRX Quantum*, 3(2):020326, May 2022.

[27] C. J. Wood and J. M. Gambetta. Quantification and characterization of leakage errors. *Physical Review A*, 97(3):032306, Mar 2018.

[28] M. Baumann and M. Braun. Hyperfine structure investigations in excited D-states of ^{171}Yb and ^{173}Yb. *Zeitschrift für Physik D - Atoms, Molecules and Clusters*, 1:247–251, 1986.